PNAS RESEARCH ARTICLE | PHYSICS

Non-Majorana modes in diluted spin chains proximitized to a superconductor

Felix Küster[a], Sascha Brinker[b,c], Richard Hess[d], Daniel Loss[d], Stuart S. P. Parkin[a], Jelena Klinovaja[d,1], Samir Lounis[b,c,e,1], and Paolo Sessi[a,1]

Edited by J. C. Davis, University of Oxford, Oxford, United Kingdom; received June 29, 2022; accepted August 31, 2022

Spin chains proximitized with superconducting condensates have emerged as one of the most promising platforms for the realization of Majorana modes. Here, we craft diluted spin chains atom by atom following a seminal theoretical proposal suggesting indirect coupling mechanisms as a viable route to trigger topological superconductivity. Starting from single adatoms hosting deep Shiba states, we use the highly anisotropic Fermi surface of the substrate to create spin chains characterized by different magnetic configurations along distinct crystallographic directions. By scrutinizing a large set of parameters we reveal the ubiquitous emergence of boundary modes. Although mimicking signatures of Majorana modes, the end modes are identified as topologically trivial Shiba states. Our work demonstrates that zero-energy modes in spin chains proximitized to superconductors are not necessarily a link to Majorana modes while simultaneously identifying other experimental platforms, driving mechanisms, and test protocols for the determination of topologically nontrivial superconducting phases.

Majorana mode | scanning tunneling spectroscopy | spin chain | proximity superconductivity | Shiba state

Significance

Spin chains coupled to superconducting condensates have been proposed as a viable route to create Majorana zero modes (MZMs). These exotic quasiparticles raised great expectations for creating fault-tolerant qubits. Experimentally, MZMs are generally detected as zero-energy boundary modes. Here, we craft distinct spin chains coupled to an elemental superconductor. In all chains, we reveal the existence of boundary modes located at zero energy. Despite showing spectroscopic signatures compatible with MZMs, our analysis allows us to identify them as local bound states induced by the magnetic exchange coupling between magnetic impurities and the superconducting condensate. Our results demonstrate how subtle mechanisms can effectively mimic signatures of MZMs, highlighting the need of additional methods for their unambiguous experimental detection.

The development of topological concepts in condensed-matter systems has motivated much interest in the realization of Majorana states (1, 2). These exotic states are predicted to emerge at boundaries of topological superconductors (3), manifesting themselves as zero-energy modes in conductance measurements (4–10). Beyond their fundamental interest, which illustrates how topological condensed-matter systems can be extremely fertile in establishing strong connections with concepts developed in the world of high-energy physics (11, 12), the associated non-Abelian exchange statistics have raised great expectations for their direct application in topological quantum computational schemes (13). Following Kitaev's seminal proposal (14), several distinct platforms have been theoretically proposed for their experimental realization, most notably based on the proximitization of a conventional s-wave superconductor to allow for spin-split states, such as by hosting them on topological insulators (15), on semiconductors with strong spin–orbit coupling (16, 17), or via magnetic nanostructures (18–20).

Since Majorana fermions are a direct manifestation of a topologically nontrivial superconducting state, they are expected to reveal themselves as boundary excitations. In this context, scanning tunneling microscopy and spectroscopy measurements are especially suitable to atomically resolve the emergence of Majorana states and to disentangle them from spurious and topologically trivial zero-bias states (5–7, 10, 21–23). Following seminal works on self-assembled magnetic chains (5–7), the recent use of atomic manipulation techniques has allowed for the construction of disorder-free chains, providing insights into the controlled creation and manipulation of Majorana states (8, 9, 24–27).

For the building blocks, several theoretical proposals have highlighted the important role of having diluted impurities with the superconducting host playing an active role in mediating their coupling (18–20). Despite the appealing prospects of the proposed topological concepts and scenarios, their experimental realization has remained elusive and largely unexplored. All systems explored so far are densely packed and ferromagnetically coupled through direct magnetic exchange (5–9, 24–26).

Here, we scrutinize dilute spin chains in which the direct hopping between d levels is weak (28, 29). We demonstrate that the presence of Yu–Shiba–Rusinov (YSR) (or Shiba) pairs very close to the center of the superconducting gap allows the emergence of modes highly localized at the ends of the chains for a large variety of parameters such as coupling strengths, magnetic configurations, hopping amplitude, and distinct unit cell. Despite displaying some spectroscopic signatures compatible with Majorana bound states, the end modes are identified as topologically trivial Shiba states energetically located at or very close to zero.

Author contributions: F.K., S.S.P.P., and P.S. designed research; F.K., S.B., R.H., D.L., J.K., S.L., and P.S. performed research; F.K., S.L., and P.S. analyzed data; and F.K., D.L., S.S.P.P., J.K., S.L., and P.S. wrote the paper.

The authors declare no competing interest.

This article is a PNAS Direct Submission.

[1]To whom correspondence may be addressed. Email: jelena.klinovaja@unibas.ch, s.lounis@fz-juelich.de, or paolo.sessi@mpi-halle.mpg.de.

This article contains supporting information online at https://www.pnas.org/lookup/suppl/doi:10.1073/pnas.2210589119/-/DCSupplemental.

Published October 10, 2022.

Results

Creation of Zero-Energy Boundary Modes. One-dimensional spin chains are created atom by atom utilizing atomic manipulation in a scanning tunneling microscope (STM) operated at cryogenic temperatures. Details on sample preparation and measurement protocols can be found in *Methods*. We focus on Cr atoms indirectly coupled through the (110) surface of niobium, a system that has recently been demonstrated to allow for the tuning of interactions by actively using the superconducting condensate to mediate indirect coupling among the localized Cr spins (29).

Fig. 1 reports the creation and spectroscopic characterization of spin chains built along the crystallographic direction $[1\bar{1}3]$, as illustrated in Fig. 1*A*. The distance between successive adatoms amounts to 0.55 nm. Fig. 1*B* illustrates the spectroscopic characterization of the atomically crafted chains for representative chain lengths up to 10 atoms. All spectroscopic measurements have been acquired using a superconducting tip. This allows us to investigate the electron–hole symmetry of the chain's zero-energy modes, which correspond to the tip superconducting energy gap $\pm\Delta_{\mathrm{tip}}$ (Fig. 1*B*, black dashed line). More spectroscopic data as well as topographic images on distinct chains can be found in *SI Appendix*, Notes 1–4.

A rich spectroscopic scenario is visible by positioning the STM tip on top of a single Cr adatom ($n = 1$) (30). Several peaks emerge within the bare Nb substrate superconducting energy gap. These peaks are direct fingerprints of magnetic impurity–superconductor interactions, with magnetic moments inducing YSR quasiparticle resonances residing inside the superconducting energy gap. YSR states always appear in pairs that are energetically particle–hole symmetric with respect to the Fermi level (31–34). As demonstrated in *SI Appendix*, Note 2, mapping their spatial distribution allows one to identify their orbital character (30, 35). In the present case, the d_{z^2} orbital dominates near the Fermi level, corresponding to a deep YSR state (20). When the magnetic impurities are brought close to each other, the YSR states undergo a shift depending on the interaction between adatoms (36, 37), with the individual YSR states hybridizing and creating the so-called Shiba bands.

When two adatoms are brought close to each other ($n = 2$), their interaction shifts the d_{z^2}-derived YSR pairs toward higher binding energies compared to the single adatom case ($n = 1$) showing higher intensity above the Fermi level (28, 29, 38). When a third atom is added ($n = 3$), spectral weight is trapped at the tip superconducting energy gap $\pm\Delta_{\mathrm{tip}}$ at the end of the chain (Fig. 1*B*, red curve), a scenario that does not change by progressively increasing the length. The YSR bands in the bulk (Fig. 1*B*, black line) do not show any significant spectral evolution, within the limit of our experimental resolution, for chains longer than $n = 6$ atoms, signaling that the asymptotic limit is reached for a very short distance. The spatial distribution of the zero-energy mode across the chain corresponds to the intensity at the tip superconducting energy gap $\pm\Delta_{\mathrm{tip}}$. It is reported in Fig. 1*C*, showing a clear enhancement at the chain's boundary over a length scale of $\sim$1 nm, which is independent of the chain length. The localization at the chain ends is also visible in

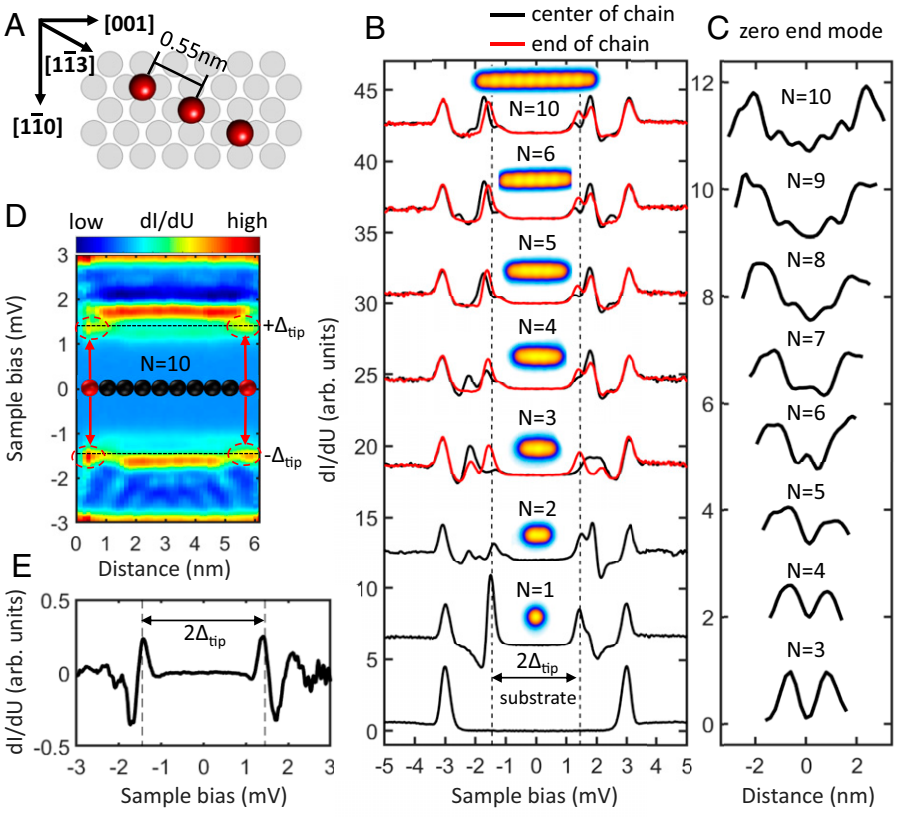

Fig. 1. Building a chain of Cr atoms, atom by atom. (*A*) Illustration of the positions of the Cr atoms (red) on the Nb lattice. Atoms are added sequentially along the $[1\bar{1}3]$ direction at a spacing of 0.55 nm. (*B*) d*I*/d*U* signal measured after sequentially adding Cr atoms to the chain, one atom at a time, up to a chain that is 10 atoms long. For chains longer than $N = 6$ up to 10 atoms, no significant changes in the energy dependence of d*I*/d*U* are observed. Black and red signals correspond to the center and end of the chains, respectively. (*C*) Spectral accumulation at zero energy (sum of intensities at $\pm\Delta_{\mathrm{tip}}$ in our case because of the use of superconducting tips) emerges at the chain ends starting from $n = 3$. (*D* and *E*) Energy-resolved d*I*/d*U* intensity for $n = 10$ visualizing the appearance of end modes (red arrows) located at $\pm\Delta_{\mathrm{tip}}$ and highlighted in *E* after subtracting the background inside the bulk of the chains.

the full spectroscopy map acquired along the chain, reported in Fig. 1*D*. When normalized by subtracting the average spectrum in the bulk of the chain, the spectrum at the chain's end shows, within the limit of our energy resolution, particle–hole symmetric peaks centered at the tip superconducting energy gap $\pm\Delta_{tip}$, as visualized in Fig. 1*E*. As illustrated in *SI Appendix*, Fig. S3, no significant change is observed on longer chains and by using different microtips. This signature would be compatible with one of the distinct fingerprints of Majorana modes. Moreover, the persistence of these modes at zero energy independently from the chain length allows us to effectively identify them as boundary modes. However, it is highly unlikely that such short chains realize a topological superconductor, an observation that indicates that they are boundary states, plausibly of trivial origin, and accidentally located at zero energy. Indeed, it is conventionally expected that at such short distances Majorana states at opposite ends hybridize and split away from zero energy (39).

Crystallographic Direction and Hopping Dependence of Boundary Modes. The electronic structure anisotropy of the Nb(110) surface (40) together with the presence of deep YSR pairs (30, 35) offers a unique opportunity to experimentally scrutinize different experimental scenarios. Indeed, spin chains built along various crystallographic directions are characterized by distinct spacing among the atoms, resulting in different interaction strengths and magnetic ground states and, consequently, a topological phase diagram (*Discussion*). Moreover, by varying the interatomic spacing inside the chain, it is possible to experimentally vary the hopping amplitude. Overall, this supplies unprecedented flexibility to controllably explore the formation of YSR bands and the emergence of boundary modes in a large experimental parameter space. To shed light on these aspects, Fig. 2 analyzes chains consisting of 15 adatoms aligned along three distinct crystallographic directions. As schematically illustrated in Fig. 2*A*, the interatomic spacing is 0.66, 0.57, and 0.93 nm along [001], [1$\bar{1}$1], and [1$\bar{1}$0] directions, respectively.

Fig. 2 *B–D* reports the spectroscopic mapping of the superconducting state induced in each one of the chains. Its inspection reveals that, despite each direction being characterized by distinct spectroscopic signatures, all chains show spectral weight accumulation at or very close to $\pm\Delta_{tip}$ localized at their ends (Fig. 2 *B–D*, dashed lines). This effect can be visualized in two distinct ways: 1) by directly comparing spectra acquired by positioning the tip in the center of the chain (black curve) and at the chain end (red curve), as illustrated in Fig. 2 *E–G*, and 2) by mapping the spatial distribution of the spectral intensity at zero energy (sum of the spectral weight at $\pm\Delta_{tip}$ because of the superconducting tip energy gap) as shown in Fig. 2 *H–J*. Additional spectroscopic data confirming the spectral weight accumulation at zero energy also for shorter chains are reported in *SI Appendix*, Note 5.

The bandwidth of Shiba bands can be directly controlled by acting on the hopping amplitude determined by interatomic spacing. This concept is illustrated in Fig. 3 for chains assembled along the [1$\bar{1}$1] direction, i.e., the direction characterized by the smallest possible discrete distance between adatoms. These chains correspond to the experimental realization of the distinct configurations illustrated in Fig. 3*A*. By increasing the distance between the adatoms, the hopping amplitude is progressively reduced. Our spectroscopic results, reported Fig. 3 *B–J*, show that the strong accumulation of spectral weight predominantly localized at the end of the chains becomes progressively weaker by increasing the distance between adatoms. For distances of ∼1.43 nm (Fig. 3 *D*, *G*, and *J*), the data reveal a scenario where adatoms are essentially decoupled, as evidenced by the very small differences visible in the spectroscopy once comparing data acquired inside the chain and at the chain end. Interestingly, a distinct boundary

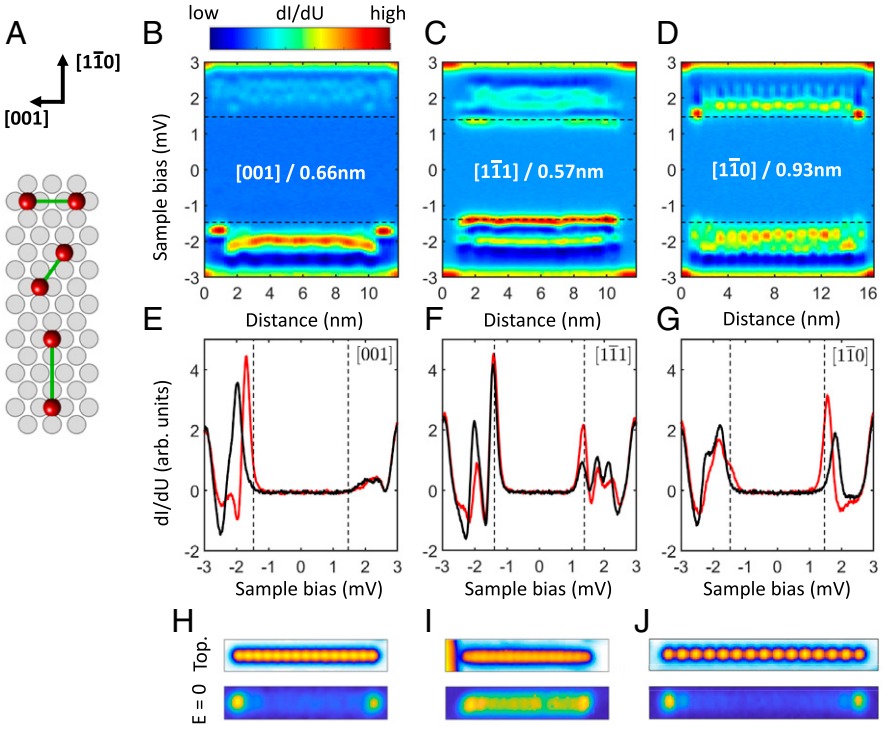

Fig. 2. Spin chains along different crystallographic directions. (*A*) Illustration of the Cr atom positions (red) on the Nb lattice for three different alignments. In each case a green line shows the connections between the atoms. (*B–D*) Spectroscopic mapping along the chains for each of the scenarios illustrated in *A*. (*E–G*) Comparison of spectra acquired by positioning the tip in the center of the chain (black curve) and at the chain end (red curve). Black dashed lines correspond to the tip superconducting gap $\pm\Delta_{tip}$. (*H–J*) Topography (*Top* panels) and spectroscopy map (*Bottom* panels) revealing an accumulation of spectral weight at zero energy (sum of the intensities at $\pm\Delta_{tip}$ because of the superconducting tip energy gap) localized at the chain's end. All chains consist of 15 atoms.

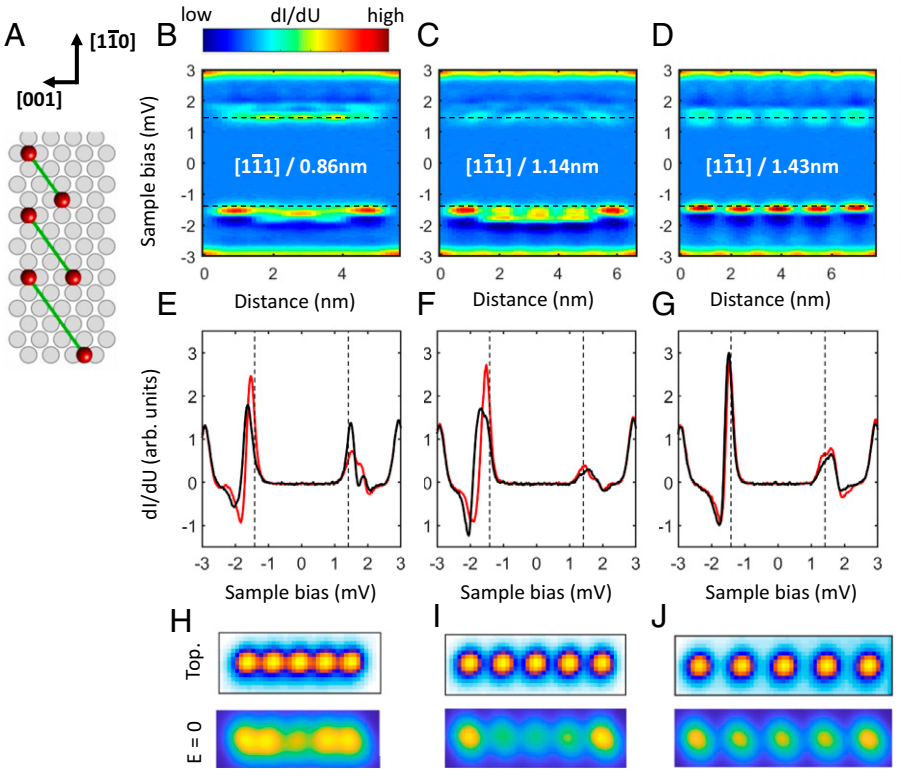

Fig. 3. Influence of hopping amplitude. (*A*) Illustration of the Cr atom positions (red) on the Nb lattice for different spacing between adatoms along the [1$\bar{1}$1] crystallographic direction. In each case a green line shows the connections between the atoms. (*B*–*D*) Spectroscopic mapping of short chains with adatoms placed at a progressively larger distance, corresponding to the scenarios illustrated in *A*. (*E*–G) Comparison of spectra acquired by positioning the tip in the center of the chains (black curve) and at the chain end (red curve). Black dashed lines correspond to the tip superconducting gap $\pm\Delta_{tip}$. (*H*–*J*) Topography (*Top* panels) and spectroscopy map (*Bottom* panels) at zero energy (sum of the intensities at $\pm\Delta_{tip}$ because of the superconducting tip energy gap).

behavior at zero energy is also found in the metallic regime (41) (*SI Appendix*, Note 6 and *Discussion* below).

Dimerized Chains. To scrutinize the origin of the zero-energy end modes, we experimentally assembled chains where the unit cell consists of two adatoms. Despite its importance in clarifying the origin of the end modes, this scenario has not been explored to date, with all previous works focusing on chains consisting of equally spaced nearest-neighboring adatoms (5–9, 24). As schematically illustrated in Fig. 4*A*, a two-atom unit cell structure is achieved by periodically placing adatoms at two distinct distances corresponding to two distinct hopping amplitudes. Fig. 4*B* shows a topographic image of the resulting spin chain, which consists of 10 unit cells assembled using 20 atoms. The spectroscopic measurements visualize a stronger accumulation of spectral weight at the tip superconducting gap "localized at the ends of the chain" (Fig. 4*B*, black dashed lines). This is highlighted by the zero-energy map and its relative line profile (because of the tip superconducting energy gap, the zero-energy spectral weight of the chains corresponds to the sum of the intensities at $\pm\Delta_{tip}$). The localization of the end modes still takes place on a very short length scale (see zero-energy maps in Fig. 4). To clarify the origin of the zero-energy modes, we tested their robustness against perturbations. This is illustrated in Fig. 4 *C* and *D*. Fig. 4*C* shows a chain where an additional adatom is placed inside the bulk that acts as a structural and electronic defect, acting as a domain wall. If the zero-energy spectral intensity highly localized at the end of the chain would be a Majorana mode, we might expect to observe four: two at the chain ends and two more on the right and on the left of the domain wall, because the domain wall would cut the topological superconductors into two, which is not in line with our observation. However, a more complex scenario cannot be excluded. Indeed, the chain end and the domain wall are not fully equivalent cases. The defect provides a perturbation as well as a continuity in the electronic structure, which makes it distinct with respect to the chain end. In Fig. 4*D*, additional single adatoms have been connected to the ends of the chains. The spectral weight accumulation at zero energy remains localized at the chain end. However, a higher spectral intensity at zero is now observed on both the dimer and the last adatom. Since the bulk of the wire has not been modified, which dictates the topological properties and the intrinsic spatial extension of possible Majorana modes, their localization should not be altered by changing the edge.

Origin of Zero-Energy Modes. In the following we explore theoretically whether the investigated finite chains can host Majorana states by building up a minimal tight-binding model (details in *SI Appendix*, Note 7). In particular, we consider the trivial regime by neglecting the spin–orbit interaction (SOI). For a single magnetic impurity, the experimental data reveal a deep YSR state close to zero energy (*SI Appendix*, Note 2). This occurs for a certain $s-d$ exchange coupling strength $J=J_c$, between the adatom's spin and that of the surface electrons, which we fix in our model, unless stated otherwise. Adding further nearby magnetic impurities leads to hybridization and energy splitting of the YSR states as a function of their overlap, which is determined by the distance L between the impurities. If the impurities are deposited close to each other, e.g., separated only by one lattice spacing, the energy of the lowest subgap state strongly oscillates as a function of the chain length, as shown in Fig. 5*A*. For specific chain lengths, the lowest-energy state can be experimentally detected as a zero-energy mode if the finite-energy resolution is taken into account. Moreover, the probability density of the lowest subgap state and the local density of states (LDOS) (which accounts also for higher

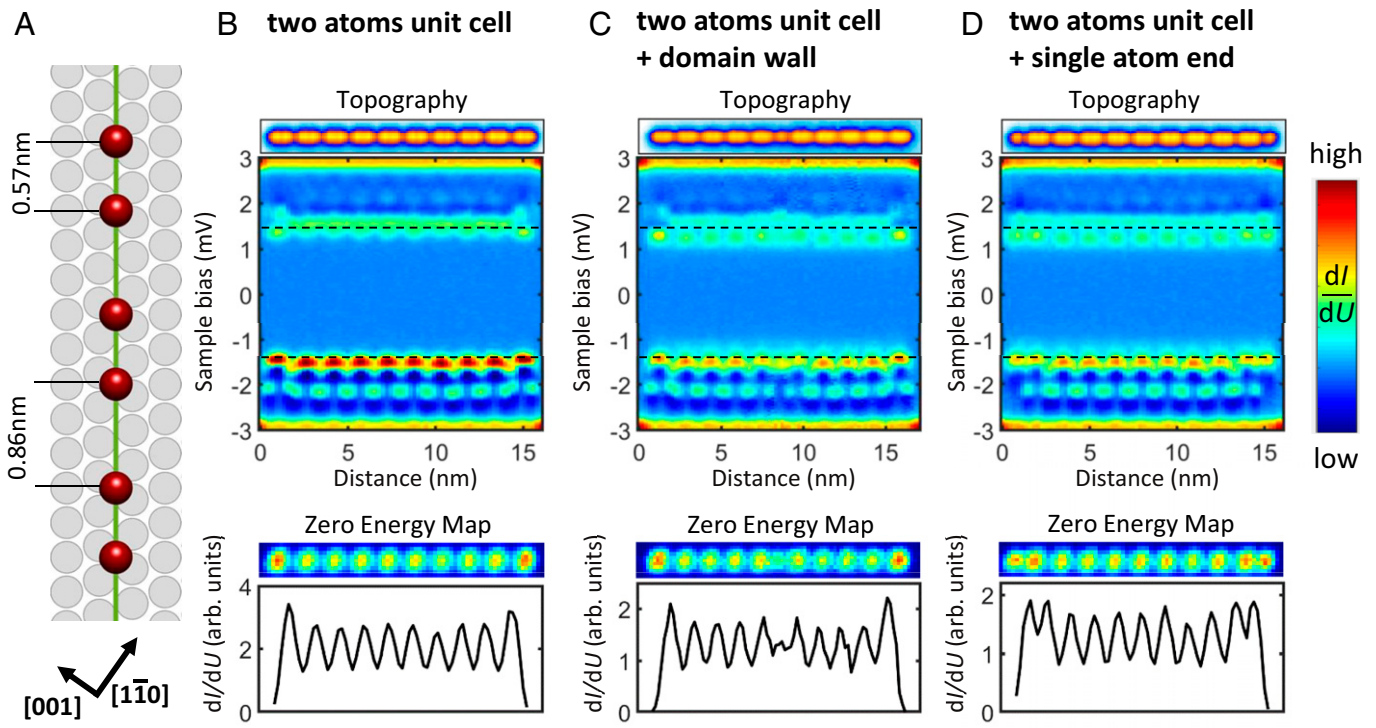

Fig. 4. Distinct unit cells and robustness against perturbations. (*A*) Schematic illustration of a two-atoms unit cell spin chain. (*B–D*) Topography (*Top* panels), spectroscopic mapping with the dashed lines corresponding to the tip superconducting gap (*Middle* panels), and zero-energy spatial map with corresponding line profile (*Bottom* panels) for (*B*) the pristine chain, (*C*) the chain with internal perturbation, and (*D*) the chain with perturbation at the end. Zero-energy end modes (corresponding to the sum of the intensities at $\pm\Delta_{\text{tip}}$ because of superconducting tip energy gap) are visible for all chains.

states due to the finite-energy broadening ϵ) are both characterized by large weights on the ends of the chain, as illustrated in Fig. 5*D*.

Next, we consider well-separated impurities at a distance $L = 5a$ to simulate the experimental scenario scrutinized in the present study, i.e., the indirectly coupled regime. In this case, the splitting is much weaker and the resulting YSR band appears narrow and localized around zero energy, as shown in Fig. 5*B*. In other words, the system hosts states with almost zero energy independent of the length of the chain. For some parameter choices the probability density of the lowest subgap state along the chain reveals large weights even on the ends of the chains (Fig. 5*E*), matching the experimental observation (Figs. 1 and 2). Since the YSR states in the model are energetically close to each other, we calculate the LDOS with a broadening parameter ϵ to account for the finite experimental energy resolution. The LDOS reveals, similar to the probability density, large peaks at the ends of the chain (Fig. 5*E*), effectively reproducing the experimental observations. Therefore, without claiming that the experimental

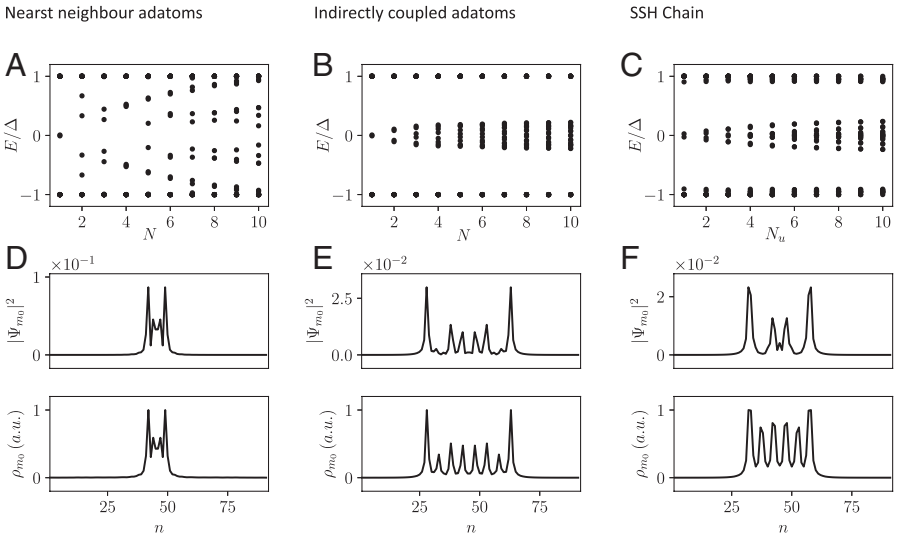

Fig. 5. Energies and wave functions for different impurity chain configurations. (*A*, *B*, *D*, and *E*) The adatoms are separated by a distance (*A* and *D*) $L = a$ and by a distance (*B* and *E*) $L = 5a$. (*C* and *F*) The impurities are ordered in unit cells: Each unit cell contains two adatoms. We set the intraunit cell distance between the two adatoms to $L = a$ and the spatial separation between the unit cells to $L = 4a$. (*A–C*) Forty lowest energies (*A* and *B*) as a function of the number of impurities N and (*C*) as a function of the number of unit cells N_u. (*D–F*) Probability density and LDOS at zero energy at the cross-section of the chain. The parameters used are $t = 1$, $\Delta = 0.2$, $\mu = 1$, $\epsilon = 0.01$ and the total size is $N_x \times N_y = 50 \times 92$. Furthermore, we used $J = J_c \approx 2.47$ in *A*, *B*, *D*, and *E* and $J = J_< \approx 1.88$ in *C* and *F*.

situation is exactly captured by the minimal tight-binding model, we conclude that trivial mechanisms can lead to effects similar to those observed in the experiments.

Finally, we order the impurities in unit cells. In particular, two impurities are separated by one lattice spacing a in each unit cell and the unit cells are separated by a distance of $L = 4a$. To find trivial zero-energy states, we start by calculating the energies of a system consisting of one unit cell as a function of the exchange coupling strength. The two overlapping YSR states have zero energy at $J_<$ and $J_>$, respectively, with $J_< < J_c < J_>$. Finally, we set the exchange coupling strength to $J_<$ and calculate the energies as a function of the number of unit cells N_u. The unit cells are well separated and a narrow band forms around zero energy, as shown in Fig. 5*C*. The probability density of the lowest state has again strong weights on the ends of the chain and the LDOS (Fig. 5*F*) looks similar to the experimental dI/dU zero-energy map reported in Fig. 4*B*. We note that the effect of having a higher intensity at the end is not generally valid for the probability density of the lowest state; i.e., for other chain lengths the weight can be distributed differently. However, the LDOS, which takes multiple states close to zero energy into account, has almost the same shape also for varying chain length, namely peaks at the positions of the unit cells at slightly higher peaks at the ends of the chain.

Discussion

Our work systematically scrutinizes dilute spin chains proximitized to a superconducting condensate. Contrary to earlier studies on densely packed adatoms (5–9, 24, 26), we focus on the dilute regime, which allows us to minimize the direct hopping inside the wire. Starting from single adatoms hosting deep Shiba states, we use the highly anisotropic Nb(110) Fermi surface to create distinct Shiba bands. In all chains, we reveal the emergence of highly localized boundary modes showing some spectroscopic signatures in agreement with expectations for Majorana modes. However, these are identified as trivial Shiba states characterized by a larger spectral weight localized at the chain end.

Even if in theory the chains are made long enough (beyond our current experimental reach), a map of the topological invariants for infinite Cr wires along distinct crystallographic directions and characterized by different magnetic states (see Fig. 6*A*; *Methods*; and *SI Appendix*, Note 8 for more details) clearly indicates the sensitivity of the topological behavior on the details of the electronic structure. This is illustrated in Fig. 6*B*, which summarizes the results of multiorbital tight-binding simulations parameterized ab initio and including the proximity-induced superconductivity as a parameter (*SI Appendix*, Note 9). Very small topologically nontrivial regions (blue areas) appear for the $[1\bar{1}0]$ chain, which is characterized by weak hopping and flat electronic bands. Increasing the hopping amplitude enlarges the bandwidths and the size of the topological nontrivial regions, as can be seen in the $[1\bar{1}1]$, $[1\bar{1}3]$, and $[001]$ chains. For the latter, the hopping is comparable to the crystal field splitting, leading to an overlap of the different bands and a complex phase diagram. This shows that, even if the wires are made long enough, entering into a topologically nontrivial regime is challenging once considering the complexity of real materials. It requires fine control of different parameters such as exchange splitting, position of d-orbital, range of hopping, and crystal field splitting.

Overall, our results imply that zero-bias, length-independent, boundary modes are not necessarily linked to Majorana modes.

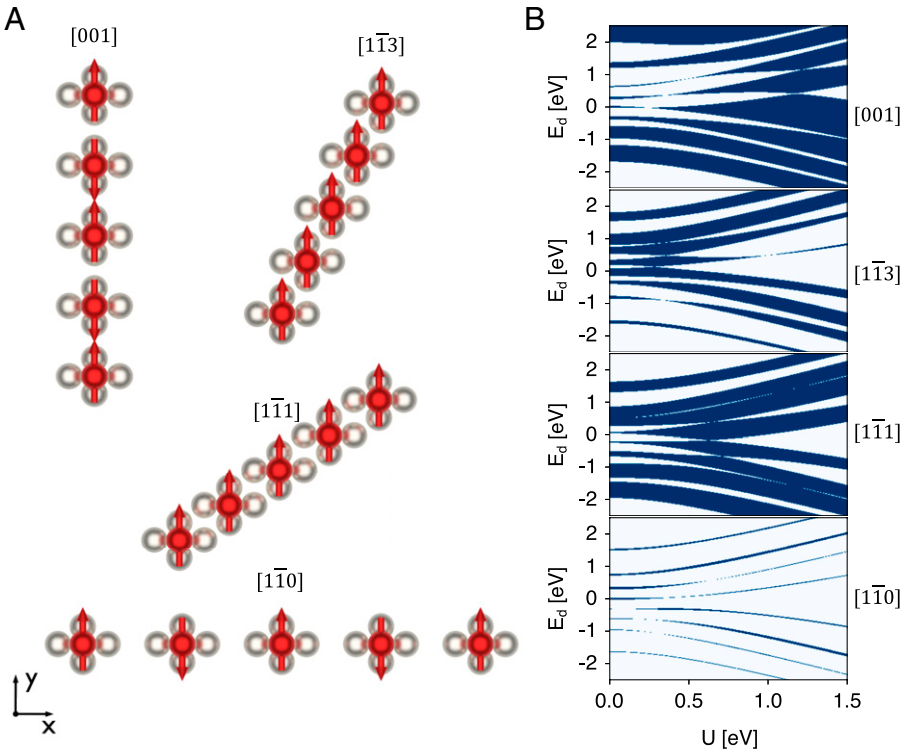

Fig. 6. Topological properties and magnetic ground states of the different Cr chains deposited on the Nb(110) surface. Shown are the [001], [1$\bar{1}$3], [1$\bar{1}$1], and [1$\bar{1}$0] directions. (*A*) Magnetic structures obtained from first principles (*Methods*). (*B*) Phase diagrams of the Majorana number for the infinite wires as a function of the spin splitting U and the energy of the d-orbitals E_d and including hopping up to four nearest neighbors. The range of hopping can induce destructive or constructive interference effects. For example, the nontrivial regions are amplified by considering four neighbors instead of only nearest neighbors for the [001] chain, while they are reduced in size for the [1$\bar{1}$0] chain. Topological regions are shown in blue, while the trivial nontopological regions are white. For more details see *SI Appendix*, Notes 8 and 9.

At the same time, by using indirect coupling mechanisms on anisotropic surfaces, we demonstrate that it is possible to significantly enlarge the experimental parameter space, opening additional routes for the experimental search of topologically nontrivial superconducting states.

Methods

Sample and Tip Preparation. A clean Nb(110) substrate was obtained by flashing the crystal to 2,300 K in 12 s (42) hundreds of times. Measurements were taken at a temperature T = 600 mK using the Tribus STM head (Scienta Omicron). Cr adatoms were deposited in situ using an e-beam evaporator while keeping the sample below a temperature of 15 K. All atoms were found to be adsorbed in the hollow site of the Nb(110) surface (30). Cr chains have been assembled by the atomic manipulation technique by dragging them with the STM tip in constant current mode using a setpoint of V = −5 mV; I = 70 nA. dI/dU spectra were acquired by standard lock-in technique. To enhance the energy resolution, we used superconducting Nb tips obtained by deep indentations into the Nb single crystal.

First-Principles and Tight-Binding Model Calculations. The ab initio simulations are based on the scalar-relativistic full-electron Korringa–Kohn–Rostoker (KKR) Green's function augmented self-consistently with spin–orbit interaction (43, 44). The theoretical framework uses multiple-scattering theory allowing an embedding scheme, which is ideal to address the electronic and magnetic properties of nanostructures in real space without the use of periodic supercells. We utilize the atomic-sphere approximation (ASA) and consider the full charge density within the local spin density approximation (LSDA) (45). We assume an angular momentum cutoff at $\ell_{max} = 3$ for the orbital expansion of the Green's function and when extracting the local density of states a k-mesh of 150 × 150 is considered. The Nb(110) surface is modeled by a slab containing 22 layers enclosed by two vacuum regions with a thickness of 9.33 Åeach. Due to the large spacings between the atoms of the Cr chains, we use the geometrical properties obtained for isolated Cr adatoms. Thus, the chain atoms are placed on the hollow stacking site relaxed toward the surface by 20% of the interlayer distance of the underlying Nb(110) surface, which was shown to be the energetically favored stacking for isolated adatoms in ref. 30.

Due to the large distances between the Cr atoms in all chains, we find negligible boundary effects in the electronic and magnetic ground-state structures of the chains. The magnetic moments of approximately 3.0 μ_B per atom are uniformly distributed with a difference of less than 0.02 μ_B between the edge and the central atoms for all chains.

To describe the magnetic structure of the chains we use the generalized Heisenberg model,

$$H = \sum_i \mathbf{e}_i \mathcal{K}_i \mathbf{e}_i + \frac{1}{2}\sum_{ij} J_{ij}\mathbf{e}_i \cdot \mathbf{e}_j + \frac{1}{2}\sum_{ij} \mathbf{D}_{ij} \cdot (\mathbf{e}_i \times \mathbf{e}_j), \qquad [1]$$

where $\mathcal{K}_i$ is the on-site anisotropy, J_{ij} is the isotropic exchange interaction, and $\mathbf{D}_{ij}$ is the Dzyaloshinskii–Moriya interaction between the ith and the jth atom with the magnetic moment $\mathbf{m}_i = m_i\mathbf{e}_i$. The magnetic exchange interactions were obtained using the magnetic force theorem in the frozen-potential approximation and the infinitesimal rotation method (46, 47). The on-site magnetic anisotropy of the Cr atoms in all chains is obtained from the method of constraining fields (48) and was found to be similar to the one of the isolated adatoms reported in ref. 30. Further information can be found in *SI Appendix*, Note 4.

The different chains exhibit fundamentally different magnetic exchange interactions among nearest-neighboring adatoms, ranging from antiferromagnetic coupling of $J = 2.1$ meV for the $[1\bar{1}0]$ chain and $J = 11.5$ meV for the [001] chain to ferromagnetic coupling of $J = -6.2$ meV for the $[1\bar{1}1]$ chain and $J = -1.7$ meV for the $[1\bar{1}3]$ chain. Minimizing a Heisenberg model with the magnetic exchange parameters from first principles leads to the ground states of the chains shown in Fig. 6*A*. Due to the weak Dzyaloshinskii–Moriya interaction, the chains are almost collinear and follow the ferromagnetic and antiferromagnetic couplings dictated by the isotropic exchange (see *Methods* and *SI Appendix*, Note 6 for more details).

The topological invariant is calculated using a multiorbital tight-binding model with parameters obtained from density functional theory and an effective Hamiltonian construction (see ref. 24 and *SI Appendix*, Note 7).

Note. After completing our work, we became aware of a STM-based study on diluted chains of Fe atoms coupled to superconducting $NbSe_2$ (49).

Data, Materials, and Software Availability. All study data are included in the article and/or *SI Appendix*.

Author affiliations: [a]Nano-Systems from Ions, Spins, and Electrons (NISE) Department, Max Planck Institute of Microstructure Physics, 06120 Halle, Germany; [b]Peter Grünberg Institut, Forschungszentrum Jülich & JARA, D-52425 Jülich, Germany; [c]Institute for Advanced Simulation, Forschungszentrum Jülich & Jülich Aachen Research Alliance (JARA), D-52425 Jülich, Germany; [d]Department of Physics, University of Basel, CH-4056 Basel, Switzerland; and [e]Faculty of Physics, University of Duisburg-Essen and Center for Nanointegration Duisburg-Essen (CENIDE), 47053 Duisburg, Germany

1. J. Alicea, New directions in the pursuit of Majorana fermions in solid state systems. *Rep. Prog. Phys.* **75**, 076501 (2012).
2. C. Beenakker, Search for Majorana fermions in superconductors. *Annu. Rev. Condens. Matter Phys.* **4**, 113–136 (2013).
3. M. Sato, Y. Ando, Topological superconductors: A review. *Rep. Prog. Phys.* **80**, 076501 (2017).
4. V. Mourik *et al.*, Signatures of Majorana fermions in hybrid superconductor-semiconductor nanowire devices. *Science* **336**, 1003–1007 (2012).
5. S. Nadj-Perge *et al.*, Topological matter. Observation of Majorana fermions in ferromagnetic atomic chains on a superconductor. *Science* **346**, 602–607 (2014).
6. M. Ruby *et al.*, End states and subgap structure in proximity-coupled chains of magnetic adatoms. *Phys. Rev. Lett.* **115**, 197204 (2015).
7. R. Pawlak *et al.*, Probing atomic structure and Majorana wavefunctions in mono-atomic Fe chains on superconducting Pb surface. *npj Quantum Inf.* **2**, 16035 (2016).
8. H. Kim *et al.*, Toward tailoring Majorana bound states in artificially constructed magnetic atom chains on elemental superconductors. *Sci. Adv.* **4**, eaar5251 (2018).
9. A. Kamlapure, L. Cornils, J. Wiebe, R. Wiesendanger, Engineering the spin couplings in atomically crafted spin chains on an elemental superconductor. *Nat. Commun.* **9**, 3253 (2018).
10. J. P. Xu *et al.*, Experimental detection of a Majorana mode in the core of a magnetic vortex inside a topological insulator-superconductor $bi_2te_3/nbse_2$ heterostructure. *Phys. Rev. Lett.* **114**, 017001 (2015).
11. E. Majorana, Teoria simmetrica dell'elettrone e del positrone. *Il Nuovo Cimento (1924-1942)* **14**, 171 (2008).
12. F. Wilczek, Majorana returns. *Nat. Phys.* **5**, 614–618 (2009).
13. J. Alicea, Y. Oreg, G. Refael, F. von Oppen, M. P. A. Fisher, Non-Abelian statistics and topological quantum information processing in 1d wire networks. *Nat. Phys.* **7**, 412–417 (2011).
14. A. Y. Kitaev, Unpaired Majorana fermions in quantum wires. *Phys. Uspekhi* **44**, 131–136 (2001).
15. L. Fu, C. L. Kane, Superconducting proximity effect and Majorana fermions at the surface of a topological insulator. *Phys. Rev. Lett.* **100**, 096407 (2008).
16. R. M. Lutchyn, J. D. Sau, S. Das Sarma, Majorana fermions and a topological phase transition in semiconductor-superconductor heterostructures. *Phys. Rev. Lett.* **105**, 077001 (2010).
17. Y. Oreg, G. Refael, F. von Oppen, Helical liquids and Majorana bound states in quantum wires. *Phys. Rev. Lett.* **105**, 177002 (2010).
18. S. Nadj-Perge, I. K. Drozdov, B. A. Bernevig, A. Yazdani, Proposal for realizing Majorana fermions in chains of magnetic atoms on a superconductor. *Phys. Rev. B Condens. Matter Mater. Phys.* **88**, 020407 (2013).
19. J. Klinovaja, P. Stano, A. Yazdani, D. Loss, Topological superconductivity and Majorana fermions in RKKY systems. *Phys. Rev. Lett.* **111**, 186805 (2013).
20. F. Pientka, L. I. Glazman, F. von Oppen, Topological superconducting phase in helical Shiba chains. *Phys. Rev. B Condens. Matter Mater. Phys.* **88**, 155420 (2013).
21. S. Kezilebieke *et al.*, Topological superconductivity in a van der Waals heterostructure. *Nature* **588**, 424–428 (2020).
22. Z. Wang *et al.*, Evidence for dispersing 1D Majorana channels in an iron-based superconductor. *Science* **367**, 104–108 (2020).
23. E. Prada *et al.*, From Andreev to Majorana bound states in hybrid superconductor–semiconductor nanowires. *Nat. Rev. Phys.* **2**, 575–594 (2020).
24. L. Schneider *et al.*, Controlling in-gap end states by linking nonmagnetic atoms and artificially-constructed spin chains on superconductors. *Nat. Commun.* **11**, 4707 (2020).
25. L. Schneider *et al.*, Topological Shiba bands in artificial spin chains on superconductors. *Nat. Phys.* **17**, 943–948 (2021).
26. C. Mier *et al.*, Atomic manipulation of in-gap states in the $\beta - bi_2Pd$ superconductor. *Phys. Rev. B* **104**, 045406 (2021).
27. L. Schneider *et al.*, Precursors of Majorana modes and their length-dependent energy oscillations probed at both ends of atomic Shiba chains. *Nat. Nanotechnol.* **17**, 384–389 (2022).
28. H. Ding *et al.*, Tuning interactions between spins in a superconductor. *Proc. Natl. Acad. Sci. U.S.A.* **118**, e2024837118 (2021).
29. F. Küster, S. Brinker, S. Lounis, S. S. P. Parkin, P. Sessi, Long range and highly tunable coupling between local spins coupled to a superconducting condensate. *Nat. Commun.* **12**, 6722 (2021).
30. F. Küster *et al.*, Correlating Josephson supercurrents and Shiba states in quantum spins unconventionally coupled to superconductors. *Nat. Commun.* **12**, 1108 (2021).
31. L. Yu, Bound state in superconductors with paramagnetic impurities. *Wuli Xuebao* **21**, 75–98 (1965).
32. H. Shiba, Classical spins in superconductors. *Prog. Theor. Phys.* **40**, 435–451 (1968).

33. A. I. Rusinov, On the theory of gapless superconductivity in alloys containing paramagnetic impurities. *Sov. Phys. JETP* **29**, 1101–1106 (1969).
34. A. Yazdani, B. A. Jones, C. P. Lutz, M. F. Crommie, D. M. Eigler, Probing the local effects of magnetic impurities on superconductivity. *Science* **275**, 1767–1770 (1997).
35. D. J. Choi *et al.*, Mapping the orbital structure of impurity bound states in a superconductor. *Nat. Commun.* **8**, 15175 (2017).
36. D. K. Morr, N. A. Stavropoulos, Quantum interference between impurities: Creating novel many-body states in s-wave superconductors. *Phys. Rev. B Condens. Matter Mater. Phys.* **67**, 020502 (2003).
37. D. K. Morr, J. Yoon, Impurities, quantum interference, and quantum phase transitions in *s*-wave superconductors. *Phys. Rev. B Condens. Matter Mater. Phys.* **73**, 224511 (2006).
38. K. J. Franke, G. Schulze, J. I. Pascual, Competition of superconducting phenomena and Kondo screening at the nanoscale. *Science* **332**, 940–944 (2011).
39. T. D. Stanescu, R. M. Lutchyn, S. Das Sarma, Dimensional crossover in spin-orbit-coupled semiconductor nanowires with induced superconducting pairing. *Phys. Rev. B Condens. Matter Mater. Phys.* **87**, 094518 (2013).
40. A. Odobesko *et al.*, Anisotropic vortices on superconducting Nb(110). *Phys. Rev. B* **102**, 174502 (2020).
41. S. Brinker, F. Küster, S. S. P. Parkin, P. Sessi, S. Lounis, Anomalous excitations of atomically crafted quantum magnets. *Sci. Adv.* **8**, eabi7291 (2022).
42. A. B. Odobesko *et al.*, Preparation and electronic properties of clean superconducting Nb(110) surfaces. *Phys. Rev. B* **99**, 115437 (2019).
43. N. Papanikolaou, R. Zeller, P. H. Dederichs, Conceptual improvements of the KKR method. *J. Phys. Condens. Matter* **14**, 2799 (2002).
44. D. S. G. Bauer, *Development of a Relativistic Full-Potential First-Principles Multiple Scattering Green Function Method Applied to Complex Magnetic Textures of Nanostructures at Surfaces* (Forschungszentrum Jülich, 2014).
45. S. H. Vosko, L. Wilk, M. Nusair, Accurate spin-dependent electron liquid correlation energies for local spin density calculations: A critical analysis. *Can. J. Phys.* **58**, 1200–1211 (1980).
46. A. I. Liechtenstein, M. I. Katsnelson, V. P. Antropov, V. A. Gubanov, Local spin density functional approach to the theory of exchange interactions in ferromagnetic metals and alloys. *J. Magn. Magn. Mater.* **67**, 65–74 (1987).
47. H. Ebert, S. Mankovsky, Anisotropic exchange coupling in diluted magnetic semiconductors: Ab initio spin-density functional theory. *Phys. Rev. B Condens. Matter Mater. Phys.* **79**, 045209 (2009).
48. S. Brinker, M. d. S. Dias, S. Lounis, The chiral biquadratic pair interaction. *New J. Phys.* **21**, 083015 (2019).
49. E. Liebhaber *et al.*, Quantum spins and hybridization in artificially-constructed chains of magnetic adatoms on a superconductor. *Nat. Commun.* **13**, 2160 (2021).